

Multiphase Monte Carlo and Molecular Dynamics Simulations of Water and CO₂ Intercalation in Montmorillonite and Beidellite

Meysam Makaremi,^{1,2,3} Kenneth D. Jordan,^{1,2} George D. Guthrie,^{1,**} and Evgeniy M. Myshakin,^{1,4,*}

¹National Energy Technology Laboratory, 626 Cochrans Mill Road, Pittsburgh, Pennsylvania 15236

²Department of Chemistry, University of Pittsburgh, Pittsburgh, Pennsylvania 15260

³Department of Mechanical Engineering, University of Pittsburgh, Pittsburgh, Pennsylvania 15260

⁴AECOM, 626 Cochrans Mill Road, P.O. Box 10940, Pittsburgh, PA 15236

Abstract

Multiphase Gibbs ensemble Monte Carlo simulations were carried out to compute the free energy of swelling for Na-montmorillonite and Na-beidellite interacting with CO₂ and H₂O at pressure and temperature conditions relevant for geological storage aquifers. The calculated swelling free energy curves show stable monolayer and bilayer configurations of the interlayer species for Na-montmorillonite, while only the monolayer structure is found to be stable for Na-beidellite. The calculations show that CO₂ is intercalated into hydrated clay phases at concentrations greatly exceeding its solubility in bulk water. This suggests that expandable clay minerals are good candidates for storing carbon dioxide in interlayer regions. For Na-beidellite the CO₂ molecule distribution is mainly controlled by the position of the isomorphic substitutions, while for Na-montmorillonite the presence of the hydrated sodium ions plays an important role in establishing the CO₂ distribution.

Keywords: carbon storage, swelling clay minerals, surface chemistry, atomistic level simulations

*Corresponding author. E-mail address: Evgeniy.Myshakin@netl.doe.gov

**Present address: Los Alamos National Laboratory, P.O. Box 1663, Los Alamos, NM 87545

1. Introduction

Burning of fossil fuels releases large quantities of CO₂, a greenhouse gas, into the atmosphere, and there is compelling evidence that this is having a significant impact on the global temperature.¹ Sequestration of CO₂ in deep underground sedimentary layers is an approach widely suggested to reduce greenhouse gas emission.² In this approach, supercritical CO₂ (scCO₂) would be injected into deep rock formations. Successful sequestration depends on cap rocks being impermeable to CO₂. Cap rocks and host rock matrix can be enriched with swelling clays (smectites) such as montmorillonite and beidellite. The interaction of scCO₂ with hydrated smectites results in

intercalation of CO₂ into interlayer regions.³⁻⁶ Montmorillonite (MMT) and beidellite (BEI), which is a less common smectite clay mineral, are layered 2:1 dioctahedral phyllosilicates comprised of octahedral (*O*) sheets sandwiched between tetrahedral (*T*) sheets giving a TOT structure as show in Figure 1. In the absence of substitutions, the *T* sites are comprised of SiO₄ units and the *O* sites of AlO₆ units. Structural hydroxyl groups are also present in the coordination sphere of the octahedral metal. In 2:1 phyllosilicates one of three symmetrically unique octahedral sites is not occupied by a cation. MMT has predominant isomorphous substitutions of Al³⁺ ions by Mg²⁺ ions in the *O* sheet, while BEI samples tend to be dominated by isomorphous substitutions of Si⁴⁺ ions by Al³⁺ in the *T* sheets. Both types of substitution result in a net negative charge for the clay layer, which is balanced by interlayer cations such as Na⁺, Li⁺, and Ca²⁺. Hydration of the cations causes swelling of smectites and an increase of the *d*₀₀₁-spacing.^{7,8} In natural samples of MMT, some substitutions can also occur in the *T* and *O* sheets. Similarly, in natural samples of BEI, some substitutions occur in *O* sites. However, for simplicity we consider the ideal substitutions described above. This allows us to study the effect of location of the negative charges, exposed directly to interlayer species or screened by the silicon-oxygen polyhedra, on swelling behavior. Other factors affecting swelling behavior include the size and charge of the interlayer cations,^{9,10} the positions of the hydroxyl groups in the octahedral layer with respect to the vacancies in octahedral sites, resulting in *cis*-vacant or *trans*-vacant smectites,¹¹ and the magnitude of negative charges on the clay sheets.⁸ The expansion of smectites due to exposure to water and CO₂ improves the sealing properties of cap rocks, whereas shrinkage could lead to fracturing and undesirable release of injected CO₂ into the atmosphere.⁴

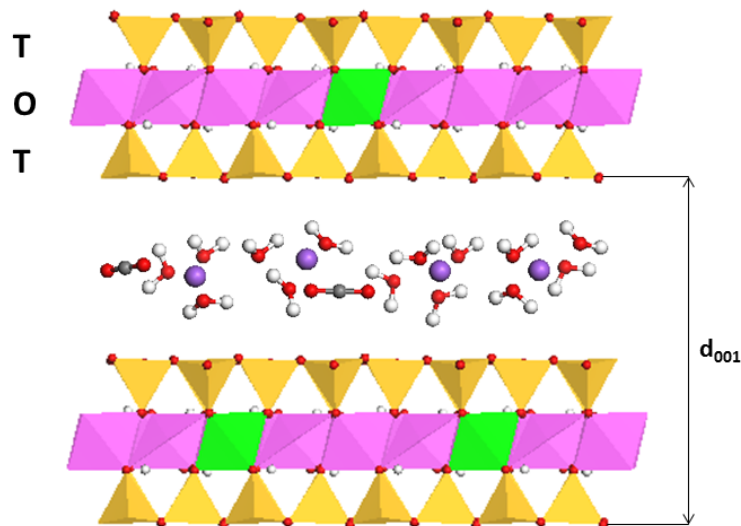


Figure 1. Smectite structure containing TOT sheets, counterions, and intercalated water and CO₂ molecules. The color coding of atoms is: purple, red, white, grey, yellow, pink and green for Na, O, H, C, Si, Al and Mg, respectively.

The swelling of smectite clays due to water intercalation is well understood from previous studies with emphasis on montmorillonite as one of the most abundant smectite minerals,¹²⁻²⁰ while beidellite has received less attention.²¹⁻²³ Previous calculations on MMT indicate that at equilibrium water can form a monolayer with basal d_{001} -spacings ranging from 11.5 to 12.5 Å (the 1W hydration state) or a bilayer with basal d_{001} -spacings ranging from 14.5 to 15.5 Å (the 2W hydration state).^{20,21,24,25} The relative stability of the 1W and 2W hydration states depends on the type of interlayer ions.²⁶ In this work “1W” and “2W” are used, respectively, to refer to the monolayer and bilayer configurations of interlayer molecules for both the pure water and for CO₂/H₂O mixtures.

Smith used Monte Carlo simulations to investigate the swelling of hydrated Cs-MMT and to calculate the immersion energy to establish the hydration state corresponding to the global free energy minimum.²⁶ The minimum was found to be consistent with the experimental result.^{27,28} In subsequent work, Young and Smith¹⁰ calculated the structural parameters for three different MMTs and found that for Cs-MMT-H₂O formation of a single water layer in the interlayer region leads to the most stable structure, while for Na-MMT-H₂O and Sr-MMT-H₂O the 2W hydration state was predicted to be more stable than 1W. The energetic contributions to the swelling free energy were calculated by Whitley and Smith,²⁹ who reported that hydration of the counter-ions plays a dominant role in the swelling behavior of MMTs.

Interaction of carbon dioxide with hydrated smectites is a complex phenomenon.^{6,30} For example, exposure of dry scCO₂ to MMT samples in the 2W and higher hydration states can induce a collapse of the d_{001} -spacing to that of the 1W state.^{6,30} On the other hand, interaction of MMT samples with wet scCO₂ promotes swelling of clays to either 1W or 2W hydration states.^{3,4,6,30}

The interaction of carbon dioxide and simple hydrocarbons with hydrated swelling clays has been studied using computer simulation methods.^{21-23,31-42} Molecular dynamics (MD) simulations have been engaged to characterize the swelling process as well as the structure and transport of interlayer species.^{36,39-42} Botan *et al.*⁴³ applied grand canonical Monte Carlo (μ VT-MC) simulations to study the effect of water and CO₂ intercalation on Na-MMT swelling at prevailing (P , T) conditions of an underground formation. They considered basal d_{001} -spacings over the range of 12

to 17 Å that excluded important d_{001} -spacings corresponding to sub-1W hydration levels. In addition, we note that the μ VT-MC method needs precise calculation of chemical potentials for the binary CO₂/H₂O mixture which is quite challenging.

The goal of the present study is to characterize intercalation of pure carbon dioxide, pure water, and CO₂/H₂O mixtures into Na-MMT and Na-BEI at two (P , T) conditions, one relevant to the geological carbon storage *via* injection of scCO₂ and the other corresponding to exposure of clay to CO₂ in the gas phase. Na-MMT and Na-BEI have different localization of the negative charges in their mineral layers allowing us to study whether this is an important factor in CO₂ uptake. The simulations employed the Gibbs ensemble Monte Carlo (GEMC) method^{44,45} in which knowledge of chemical potentials is not required to equilibrate non-interacting systems representing different phases of interest. In addition, molecular dynamics simulations in the canonical ensemble were used to analyze the properties of equilibrium water-CO₂ mixtures in the interlayer region of clays.

2. Computational Details

2.1 Swelling thermodynamics

The thermodynamics of swelling of layered materials was outlined by Diestler *et al.*⁴⁶ and Bordarier *et al.*¹⁹ As shown in those publications, the internal energy of a slit micropore can be expressed as:

$$dU = TdS + \mu dN + \sigma_{xx}s_y s_z ds_x + \sigma_{yy}s_z s_x ds_y + \sigma_{zz}s_x s_y ds_z + \tau_{zx}s_x s_y dl_x + \tau_{zy}s_x s_y dl_y. \quad (1)$$

where T , S , μ , N , σ_{ii} , τ_{ij} ($i,j = x,y,z$) are, respectively, the temperature, entropy, chemical potential, number of molecules, and normal and shear stress terms. s_i and l_i are Cartesian components of the micropore depicted in Figure 2.

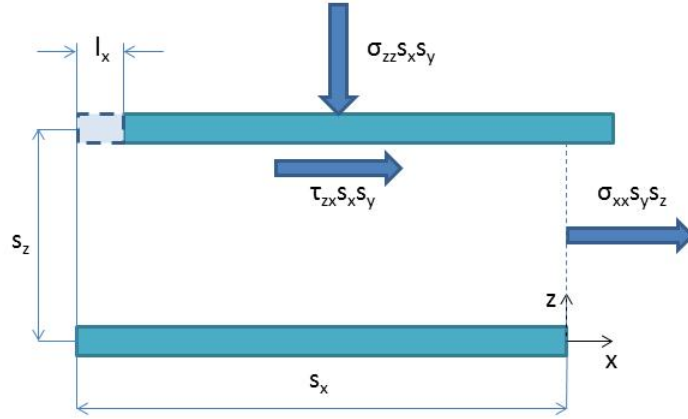


Figure 2. Slit micropore structure including position and force components.

Taking into account only the normal stress term in the z direction, the free energy, F , and isostress free energy, Φ , are defined as

$$F = U - TS - \mu N, \quad (2)$$

$$\Phi = F - \sigma_{zz} A s_z, \quad (3)$$

where A is the surface area of the slit. Thus the difference in the swelling free energy for change in wall separation Δs_z can be written as

$$\Delta\Phi = \Delta F - \sigma_{zz} A \Delta s_z \quad (4)$$

By using equations 1 and 4, eliminating the x and y directions, and also considering the fact that P and T are fixed at phase equilibrium, gives

$$\Delta\Phi = A \int_{s_z^0}^{s_z} (\sigma_{zz}(s'_z) - \sigma'_{zz}) ds'_z, \quad (5)$$

where σ'_{zz} is the applied constant stress. By eliminating the isotropic part of the stress (bulk pressure) from the stress terms, the equation can be converted into a pressure based equation

$$\Delta\Phi = -A \int_{s_z^0}^{s_z} (P_{zz}(s'_z) - P'_{zz}) ds'_z. \quad (6)$$

where $P_{zz}(s'_z)$ and P'_{zz} are the slit normal (disjoining) and the applied pressure, respectively. Equation 6 has been used by Smith²⁶ and by Botan *et al.*⁴³ to calculate the free energy of swelling as a function of the distance between layers.

2.2. Gibbs Monte Carlo Method

The use of the multiphase Gibbs approach to study equilibrium of multi-component systems is well-documented in literature.⁴⁷⁻⁵² Lopes and Tildesley⁴⁷ evaluated the multicomponent GEMC approach to calculate two-phase, three-phase and four-phase equilibria. Kristof *et al.*⁵⁰ applied the approach to the three-component, CO₂-water-methanol system at high pressure conditions, obtaining good agreement between the results of their simulations and the experimental data.

The Gibbs ensemble Monte Carlo (GEMC) method^{44,45} uses separate boxes for each phase to calculate the phase equilibrium for a target (P,T) condition and to achieve equivalence of chemical potentials of interacting species. The algorithm employs three basic trial moves: particle displacement, particle exchange, and volume change. The displacement moves include a translational or moves in a single box to satisfy temperature equilibrium. The exchange moves involve deletion of a particle in one box and its insertion into another box, to assure chemical potential equilibration. The volume moves expand or contract boxes to fulfill the pressure equilibration. Figure 3 shows the simulation setup with three boxes representing water, carbon dioxide, and clay phases.

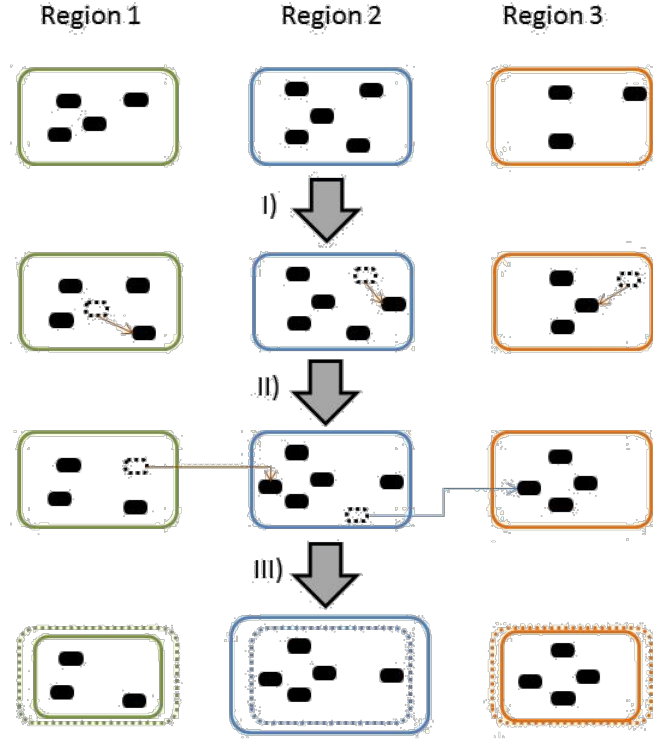


Figure 3. Illustration of Gibbs Monte Carlo method including three phases and three types of trial moves: i) displacement move, ii) exchange move, and iii) volume move.

2.3. Models and Force Fields

In this work, we used Na-MMT and Na-BEI clay structures with the stoichiometric chemical formulas $\text{Na}_{0.75}\text{Mg}_{0.75}\text{Al}_{3.25}(\text{OH})_4(\text{Si}_4\text{O}_{10})_2$ and $\text{Na}_{0.75}\text{Al}_4(\text{OH})_4(\text{Al}_{0.375}\text{Si}_{3.625}\text{O}_{10})_2$, respectively, where each clay TOT layer bears a negative charge $-0.75 |e|$ per unit cell that it is counterbalanced by interlayer Na^+ cations. The isomorphous substitutions in the TOT sheets were placed in such a way that they show a repeated pattern in the directions of a and b lattice vectors. The Al-O-Al linkage in the T sheets was avoided according to Loewenstein's rule.⁵³ The clay structure is described by the Clayff force field,²⁵ while the rigid SPC⁵⁴ and the rigid EPM2-based model of Cygan et al.³⁵ are employed for water and CO_2 , respectively. The total potential energy can be written as:

$$E_{\text{Non-bond}} = E_{\text{VDW}} + E_{\text{Coul}} + E_{\text{Stretch}}, \quad (7)$$

with

$$E_{\text{VDW}} = 4\epsilon_{ij} \left[\left(\frac{\sigma_{ij}}{r_{ij}} \right)^{12} - \left(\frac{\sigma_{ij}}{r_{ij}} \right)^6 \right], \quad E_{\text{Coul}} = \frac{q_i q_j e^2}{4\pi\epsilon_0 r_{ij}},$$

where atoms i and j are separated by a distance r_{ij} , and q_i is the charge on the atom i , e is the

elementary charge of an electron, ϵ_0 is the vacuum permittivity, and ϵ_{ij} and σ_{ij} are the Lennard-Jones energy and distance parameters, respectively. The parameters for unlike atoms were calculated by using the Lorentz-Berthelot classical combining rules.⁵⁵

$$\sigma_{ij} = \frac{1}{2}(\sigma_i + \sigma_j), \quad \epsilon_{ij} = \sqrt{\epsilon_i \epsilon_j}. \quad (8)$$

The bond stretch (E_{Stretch}) potential term is employed only for the hydroxyl groups of the clay layer and is taken to be harmonic.

2.4. Simulation methodology

The NPT-GEMC method was applied to the ternary clay-H₂O-CO₂ and binary H₂O-CO₂ systems at two (P, T) conditions, (25 bar, 348.15 K and 125 bar, 348.15 K). The binary system was included to allow comparison of the results of our calculations with previous experimental^{56,57} and computational^{43,58} data, and also to provide a reference for the subsequent simulations of the ternary system.

In the MC simulations of the Na-MMT and Na-BEI phases, 4 x 3 x 2 (20.8 x 27.6 x 2h Å) supercells, requiring 18 counterions for neutrality, were employed. Calculations were carried out for d_{001} -spacings, h , ranging from 9.5 to 18 Å in steps of 0.5 Å to cover separations ranging from nearly dry clays to the interlayer distances corresponding to the 3W hydration state. For spacings >3W, the behavior of interlayer species becomes similar to that in the bulk.¹²⁻²⁰ The MC simulations were carried out for 2x10⁵ equilibration cycles, followed by 1.5x10⁵ production cycles. Each cycle consisted of 818 attempted moves, including volume exchange, configurational-bias interbox and intrabox molecule transfer, molecule regrowth, translational, and rotational moves.⁵⁹⁻⁶¹ Exploratory calculations were carried out to determine optimal probabilities of the various types of moves with the initial values being 0.5% volume exchange, 39.5% configurational-bias consisting of both inter- and intra-box moves, 10% regrowth, and 50% displacement, including translational and rotational moves. During the exploratory simulations, the probabilities of different moves and the components in the boxes were adjusted to ensure that the calculated chemical potentials of water and CO₂ in the various phases agreed to within the standard deviations. The positions of the atoms in the clay layers were held fixed, while the Na⁺ ions were allowed to move within the interlayer space. The H₂O and CO₂ molecules were allowed to migrate between the "H₂O-rich", "CO₂-rich," and clay boxes. The cut-off radii for the non-bonded van der Waals interactions and for the real-space part of the Ewald summation of the electrostatics were chosen to be 9.5 Å, with switching distances starting from 6.5 Å

in the Ewald summation. Standard deviations of all ensemble averages were determined by the standard block average technique.⁶² The NPT-GEMC simulations were carried out using the Towhee simulation package.⁶³

In addition to the GEMC simulations described above, molecular dynamics simulations in the canonical ensemble (NVT-MD) were carried out to analyze various dynamical properties of the molecules in the clay phase. These simulations used a triclinic 8 x 4 x 4 supercell with 5120 atoms constituting the mineral portion of the clay phase. The negative charge introduced by the isomorphic substitutions is compensated by 96 sodium ions residing in all interlayers. The carbon dioxide and water content (mole fractions) were taken to correspond to those obtained for the minimum free-energy structures from the Monte Carlo simulations. Equilibration runs of 1 *ns* were carried out, followed by 5 *ns* production runs with temperature controlled by a Nse-Hoover thermostat^{64,65} with a relaxation time of 2 *ps*. The cut-off radii for the non-bonded van der Waals interactions and for the Ewald summation of the electrostatics were chosen to be 9.5 Å, with the switching distance for the latter starting from 8.5 Å. Due to the use of cut-offs for the LJ interactions, long-range dispersion corrections for energy and pressure were applied. The leap-frog algorithm⁶⁶ was used to update positions every 1 *fs*. The MD simulations were carried out using the GROMACS package.⁶⁷

The radial distribution function (RDF) for species *B* around species *A* was calculated using:

$$G_{A-B}(r) = \frac{1}{4\pi\rho_B r^2} \frac{\Delta N_{A-B}}{\Delta r}, \quad (9)$$

where ρ_B is the number density of species *B*, and ΔN_{A-B} is the average number of type *B* particles lying in the region *r* to *r* + Δr from a type *A* particle. N_{A-B} is the coordination number for *B* around *A*.

The diffusion coefficients of the interlayer species were calculated using the Einstein relation and equilibrated atomic trajectories from the NVT ensemble simulations with 1 *ps* sampling to evaluate the mean square displacement of the species of interest:

$$D = \frac{1}{6N_m t} \left\langle \sum_{j=1}^{N_m} [r_j(t) - r_j(0)]^2 \right\rangle, \quad (10)$$

where N_m is the number of the species averaged over, and $r_j(t)$ is the center-of-mass position of the *j*th species at time *t*. The averages were over 5 *ns* trajectories. The diffusion coefficients were derived from the linear slope of the mean square displacement as a function of the simulation time. Different restart points in the analysis were used to monitor convergence.

3. Results and Discussion

3.1. Monte Carlo simulations

Table 1 compares the CO₂ mole fractions and the densities of the CO₂-rich and water-rich phases of the two-phase water/CO₂ and three-phase water/CO₂/clay systems. In the latter case, calculated results are reported for both Na-MMT and Na-BEI at $d_{001} = 12.5 \text{ \AA}$.

Table 1: Mole fractions of CO₂ (X_{CO_2}) and densities (ρ) of H₂O and CO₂ in multiphase systems from previous studies and current work ($T=348.15 \text{ K}$).

system	P [bar]	$\rho \text{ [g/cm}^3\text{]}$		X_{CO_2}		
		H ₂ O	CO ₂	H ₂ O	CO ₂	clay ($d_{001}=12.5 \text{ \AA}$)
H ₂ O-CO ₂ (Experiment) ⁵⁷	25.3			0.0054	0.9818	
	126.7				0.9915	
H ₂ O-CO ₂ (μ VT-MC) ⁴³	24.2	0.934(3)	0.039(1)	0.004(1)	0.982(1)	
	122.4	0.940(5)	0.298(3)	0.014(1)	0.994(1)	
H ₂ O-CO ₂ (GEMC)	25	0.939(4)	0.040(1)	0.004(1)	0.980(4)	
	125	0.947(4)	0.314(7)	0.016(3)	0.994(2)	
MMT-H ₂ O-CO ₂ (GEMC)	25	0.937(5)	0.040(1)	0.004(1)	0.980(2)	0.014(2)
	125	0.947(5)	0.317(5)	0.016(3)	0.994(1)	0.056(2)
BEI-H ₂ O-CO ₂ (GEMC)	25	0.933(4)	0.040(1)	0.005(2)	0.983(2)	0.022(2)
	125	0.945(4)	0.321(5)	0.017(3)	0.993(1)	0.036(3)

For the CO₂/water system, the calculated mole fractions are in excellent agreement with the results of experimental measurements and with the results of grand canonical Monte Carlo simulations by Botan *et al.*⁴³ Similar mole fractions of CO₂ are found in the CO₂ and water phases of the three-phase systems as for the water/CO₂ two-phase system. Also, the densities calculated for the water-rich and CO₂-rich phases are nearly identical for the two-phase and three-phase systems. Most significantly, the concentration of carbon dioxide in the clay phase coexisting at equilibrium with the CO₂/H₂O binary system greatly exceeds that in the bulk water-rich phase.

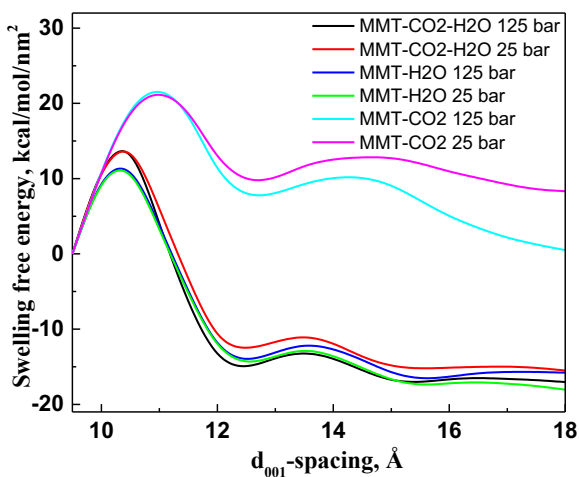


Figure 4. Calculated swelling free energy of Na-MMT as a function of the basal d_{001} -spacing for intercalation of pure CO_2 , pure H_2O , and the H_2O - CO_2 mixture at $P = 25$ and 125 bar, $T = 348.15$ K

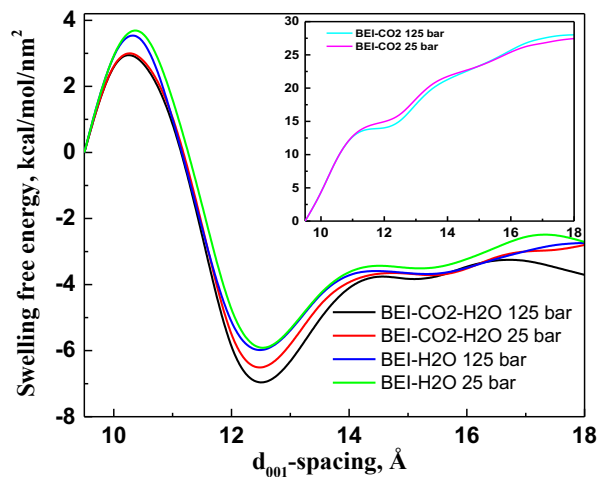


Figure 5. Calculated swelling free energy of Na-BEI as a function of the basal d_{001} -spacing for intercalation of pure CO_2 (insert), pure H_2O , and the H_2O - CO_2 mixture at $P = 25$ and 125 bar, $T = 348.15$ K.

The calculated swelling free energies as a function of the d_{001} -spacing for pure CO_2 , pure H_2O and mixed H_2O - CO_2 intercalation into Na-MMT are depicted in Figure 4. Similar profiles for Na-BEI- H_2O and Na-BEI- CO_2 - H_2O are given in Figure 5. The smallest (9.5 \AA) d_{001} -spacing in the figures corresponds to dry clays in their 0W hydration state, characterized by the absence of intercalated molecules and provides a common origin for the swelling free energy curves. From the profiles, it is seen that in the absence of water, intercalation of CO_2 is highly unfavorable thermodynamically. For Na-MMT- CO_2 the minimum at 12.5 \AA is about 10 kcal/mol/nm^2 less stable than that at 9.5 \AA , *i.e.* the 0W hydration state. This result is consistent with experimental studies that show that carbon dioxide does not intercalate into MMTs in the absence of water.^{3,30,68} Our calculations also show that, in the absence of water, intercalation of CO_2 into Na-BEI is even more unfavorable than into Na-MMT.

For the intercalation of pure water into montmorillonite, two minima corresponding to 1W and 2W are identified with energies below that of 0W. The stability of the 1W and 2W states is a consequence of ion hydration and hydrogen bonding between the intercalated water molecules and the basal oxygen atoms.⁸ The existence of two stable hydration states of Na-MMT is supported by previous studies.^{27,69-72} The present calculations predict the 2W hydration state to be more stable than

the 1W hydration state as found in earlier MC simulations^{29,73} For pure water in Na-MMT, the barrier for going from the 0W to the 1W state is calculated to be about 10 kcal/mol/nm² and is relatively insensitive to pressure. In contrast to Na-MMT-H₂O, Na-BEI-H₂O does not have a stable 2W state (Figure 5). The inability of Na-BEI-H₂O to swell beyond 1W has been documented in the literature,⁷⁴ and factors responsible for this behavior will be discussed later in Section 3.2.

The swelling free energy curves for the clay systems with intercalated binary H₂O-CO₂ mixtures display trends similar to those for pure water (Figures 4 and 5). For both Na-MMT-CO₂-H₂O and Na-BEI-CO₂-H₂O, the free energy minima at d_{001} -spacings corresponding to the 1W hydration states are deeper and the barriers separating 0W and 1W are several kcal/mol/nm² lower than those for swelling induced by pure water. For Na-MMT-CO₂-H₂O the free energy barriers between the minima at 12.5 and 15 Å spacing is calculated to be only about 3 kcal/mol/nm² with the minimum at 15.5 Å being more stable. This indicates that in geological aquifers, both mono- and bilayer arrangements of CO₂-H₂O may occur in clays rich with MMT. Increasing the pressure is found to stabilize the free-energy minima near $d_{001} = 12.5$ Å (1W) of both clay systems.

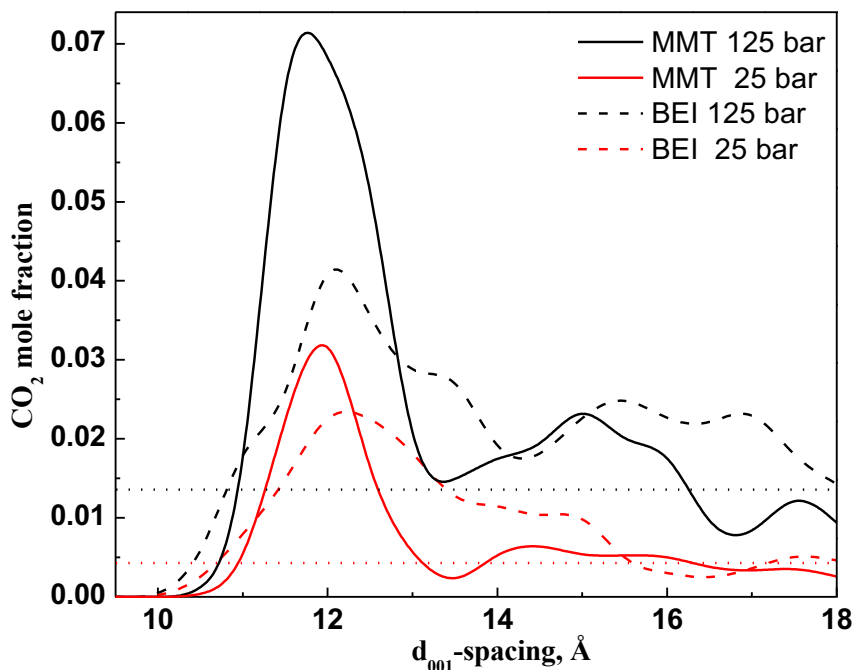


Figure 6. Equilibrium CO₂ mole fraction as a function of basal d_{001} -spacing for Na-MMT-CO₂-H₂O and Na-BEI-CO₂-H₂O at $T= 348.15$ K and $P = 25$ or 125 bar. The horizontal dotted lines represent the CO₂ mole fractions in the bulk H₂O-rich phase at $P = 125$ bar (black) and $P = 25$ bar (red), both at $T=348.15$ K.

The calculated mole fraction of CO₂ as a function of the basal d_{001} -spacing of Na-MMT and Na-BEI is reported in Figure 6. In both systems, there is a pronounced peak in the CO₂ mole fraction at a d_{001} -spacing corresponding to the 1W state and a second weaker peak (or shoulder) at a distance corresponding to 2W. Experimental studies of Na- and Ca-MMT^{3,68,75} have shown that the maximum expansion of the interlayer due to CO₂ exposure occurs at the sub 1W hydration state. Increasing the pressure causes an elevation of the CO₂ concentration in the interlayer region, with the increase being greater for Na-MMT than for Na-BEI. For both Na-MMT-CO₂-H₂O and Na-BEI-CO₂-H₂O the concentration of CO₂ in the interlayer region greatly exceeds that in the bulk water-rich phase. For Na-MMT-CO₂-H₂O, the calculated mole fractions of CO₂ in the interlayer region obtained in the present study in fairly good agreement with those reported by Botan *et al.*,⁴³ although the CO₂ concentrations predicted in this work are lower. The different concentrations may be the result of the different force fields used in the two theoretical studies.

3.2. Molecular dynamics simulations

The Na-MMT-CO₂-H₂O and Na-BEI-CO₂-H₂O systems at d_{001} -spacing of 12.5 Å (1W) and 15.5 Å (2W) equilibrated in the GEMC simulations were further characterized by molecular dynamics using the NVT ensemble. In particular, the MD simulations were used to calculate the structural and transport properties of the interlayer species. The Na-BEI-CO₂-H₂O system at $d_{001} = 15.5$ Å does not correspond to a free energy minimum and is considered primarily for comparison with Na-MMT-CO₂-H₂O at the same d_{001} -spacing.

3.2.1. Structural details of the interlayer species

Figure 7 reports for Na-MMT and Na-BEI the calculated atomic density profiles for water oxygen (O_w), carbon (C_{CO2}), and sodium ions (Na⁺) at d_{001} -spacings equal to 12.5 and 15.5 Å. The profiles were computed along the z axis (perpendicular to the clay surface) and averaged over the interlayer region of the simulation box using a 3 ns production time frame. For each species of interest, the density profiles computed for $P = 25$ and 125 bars are close agreement, and only the $P = 125$ bar data are shown in the figure. The O_w and Na⁺ density profiles for pure water are qualitatively similar to those for the H₂O/CO₂ mixtures and, therefore, are not reported.

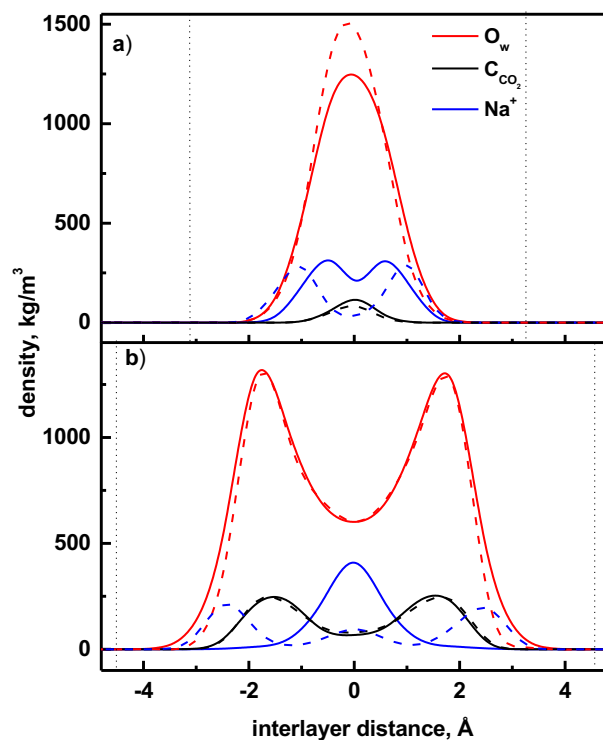


Figure 7. Density profiles of O_w , C_{CO_2} , and Na^+ along the interlayer distance perpendicular to the internal surfaces of Na-MMT- CO_2 - H_2O (solid lines) and Na-BEI- CO_2 - H_2O (dashed lines). The distributions of the intercalated species are reported for d_{001} -spacings of **a)** 12.5 Å and **b)** 15.5 Å. For **b)** the densities of C_{CO_2} are magnified by a factor of 10 for clarity. Vertical black dotted lines designate the planes of the basal oxygen atoms.

For both Na-MMT and Na-BEI, the density profiles for O_w and C_{CO_2} display a single peak in the case of $d_{001} = 12.5$ Å and two peaks in the case of $d_{001} = 15.5$ Å. For Na-MMT- CO_2 - H_2O the compositions of carbon dioxide and water in the monolayer and the bilayer structures are $\sim 4.1 H_2O / 0.3 CO_2$ and $\sim 8.9 H_2O / 0.2 CO_2$ per unit cell, respectively. These numbers are in reasonable agreement with the results of grand canonical MC simulations of Botan *et al.*⁴³ (monolayer: 3.7 $H_2O / 0.6 CO_2$ and bilayer: 8.6 $H_2O / 0.4 CO_2$ per unit cell). For Na-BEI- CO_2 - H_2O our simulations give $\sim 4.4 H_2O / 0.2 CO_2$ and $\sim 8.6 H_2O / 0.2 CO_2$ per unit cell for the monolayer and bilayer arrangement, respectively.

In an earlier paper,³⁶ we reported the d_{001} -spacing of Na-MMT as a function of the number of water molecules at fixed numbers of CO_2 molecules per unit cell in order to estimate the effect of CO_2 intercalation on the interlayer distance of Na-MMT- CO_2 - H_2O . It was deduced that the addition of 0.2-0.3 CO_2 molecules per unit cell led to an expansion of the d_{001} -spacing by ~ 0.5 - 0.6 Å. In

experimental studies performed at elevated (P, T) conditions the maximum expansion of Na-MMT upon interaction with dry scCO₂ was found at an initial d_{001} -spacing below 11.5 Å, which corresponds to a sub-1W state of hydrated Na-montmorillonite and was capped at a d_{001} -spacing equal to about 12.5 Å suggesting that expansion due to interaction with scCO₂ can be as much as ~1 Å.^{3,6} Further, Loring *et al.*⁷⁵ estimated that the maximum CO₂ absorption in the interlayer of Na-exchanged MMT occurs at water concentrations close to the transition between 0W and 1W hydration states. Thus, the values of the equilibrium concentrations of intercalated CO₂ predicted in this work appear to be somewhat underestimated.

In contrast to the density profiles of O_w and Cco₂, the density profiles of Na⁺ are quite different for Na-MMT-CO₂-H₂O and Na-BEI-CO₂-H₂O. Since the major difference in these two phyllosilicates is the location of the negative charge in the mineral layers, we conclude that this is an important factor determining the sodium ion distributions. For the $d_{001} = 12.5$ Å case, the Na⁺ density distribution is bimodal for both Na-MMT and Na-BEI. However, for Na-BEI, the positions of the peaks are shifted closer to the basal surfaces as a result of preferential coordination of sodium cations at the middle of the hexagonal rings formed by the silicon-oxygen polyhedra with isomorphic substitutions.³⁶ Effectively, the peak shift reflects a change from predominantly Na⁺ “outer-sphere” coordination with water in case of Na-MMT to “inner-sphere” adsorption at the internal clay surfaces for Na-BEI where basal oxygens participate in the first solvation shell of sodium ions. Intercalation of carbon dioxide disrupts the water network³² and also causes the Na⁺ ions to be displaced toward the clay surfaces.³⁶

In the 2W state of the Na-MMT-CO₂-H₂O system, the Na⁺ distribution peaks at the middle of interlayer. However, for Na-BEI-CO₂-H₂O, it is split into three peaks, with two more pronounced peaks corresponding to sodium ions adsorbed at the surfaces and a weaker central peak corresponding to Na⁺ ions more fully solvated by water molecules. The surface-adsorbed Na⁺ ions have in their first “solvation” shell both basal oxygens of the ditrigonal rings and interlayer water molecules. Additional information on the solvation structure of the ions can be gained by examining the radial distribution functions (RDFs) for atomic pairs of interest. Figure 8 reports the RDFs for the sodium ion – water oxygen pair computed for Na-MMT-CO₂-H₂O and Na-BEI-CO₂-H₂O at monolayer and bilayer arrangement and $P = 125$ bar. Figure 9 depicts the corresponding RDFs for the

sodium ion – basal oxygen pair. Additionally, cumulative number RDFs, *i.e.* the average number of atoms within a distance, r , were calculated.

For the monolayer arrangements of Na-MMT-CO₂-H₂O of Na-BEI-CO₂-H₂O, the Na⁺ ions are hydrated on average by 4.0 and 3.6 water molecules, respectively. On the other hand, the average number of basal O atoms directly bonded to the Na⁺ ions is 1.2 for Na-MMT, but 1.9 for Na-BEI. Thus, the total Na⁺ coordination numbers in the monolayer case is about 5.3 in both cases. For the bilayer ($d_{001}=15.5$ Å) of Na-MMT-CO₂-H₂O the Na⁺ ions tend to be coordinated by water molecules alone, achieving on average a coordination number of 5.5. On the other hand, for Na-BEI-CO₂-H₂O in the 2W state, the average Na⁺ coordination number, 5.7, derives from 4.3 of water oxygens and 1.4 of basal oxygens (Figure 9). A simulation of sodium ions in bulk water using the same (P,T) conditions and force fields as used in the clay simulations gives an average Na⁺ coordination number 5.6 for the first hydration shell, essentially the same as that calculated for Na⁺ in the bilayer in Na-MMT. Experimental studies of Na⁺ in bulk water lead to Na⁺ coordination numbers in the range 4.4-5.4^{76,77} consistent with the results of CPMD simulations⁷⁸ which give an average coordination number of 4.9 at 300K. Thus, it appears that our simulations tend to slightly overestimate the average number of water molecules coordinating the Na⁺ ions. This probably reflects a deficiency of the force field used in the simulations.

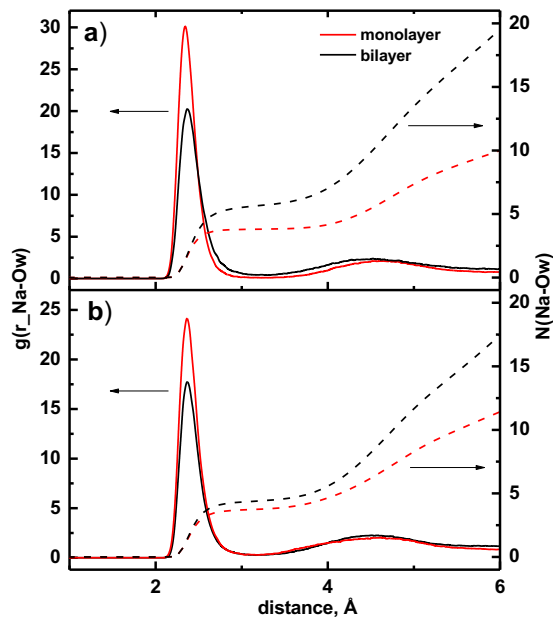


Figure 8. Radial distribution functions (solid curves) and cumulative number RDFs (dashed curves) of the $\text{Na}^+\text{-O}_w$ pair for **a)** Na-MMT- $\text{CO}_2\text{-H}_2\text{O}$ and **b)** Na-BEI- $\text{CO}_2\text{-H}_2\text{O}$ at $P = 125$ bar and $T=348.15$ K. Dotted lines designate the cumulative number RDF, *i.e.* the average number of particles within a $\text{Na}^+\text{-O}_w$ distance.

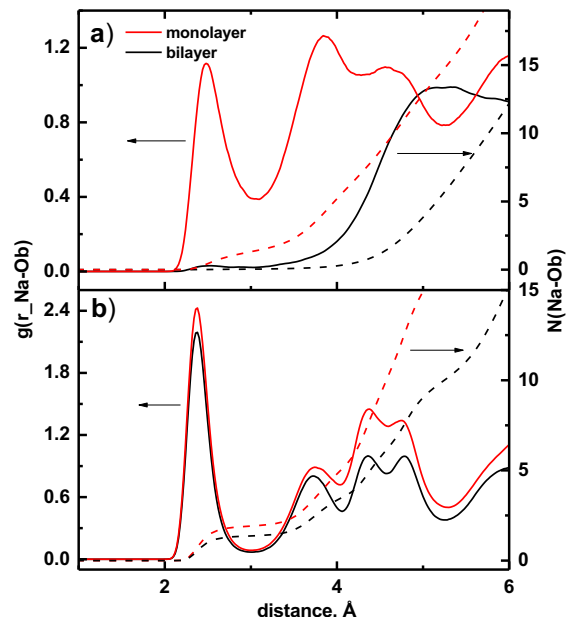


Figure 9. Radial distribution functions (solid curves) and cumulative number RDFs (dashed curves) of the $\text{Na}^+\text{-O}_b$ pair for **a)** Na-MMT- $\text{CO}_2\text{-H}_2\text{O}$ **b)** Na-BEI- $\text{CO}_2\text{-H}_2\text{O}$ at $P = 125$ bar and $T=348.15$ K. the cumulative number RDF, *i.e.* the average number of particles within a $\text{Na}^+\text{-O}_b$ distance.

In Na-BEI the strong electrostatic interaction between ions and the surfaces makes it more favorable for the cations to be adsorbed at a surface than to be located at the middle of the interlayer. In Na-MMT, in which the negative charges are screened by the *T* sheets, the Na^+ ions are more stable near the center of the bilayer where they are essentially fully hydrated. Suter *et al.*²¹ explored the thermodynamics of Li^+ , Na^+ and K^+ -montmorillonite and beidellite using *ab initio* molecular dynamics. These authors found that smectites with the free energy minimum in the middle of the interlayer for bilayer swell to the 2W hydration state with the ions forming a full hydration sphere. In Na-beidellite the position of the lowest energy region remains unchanged from monolayer to bilayer indicating that swelling would stop at monolayer. At that position, basal oxygens form a part of sodium hydration sphere. Thus, the interplay between the hydration of counter-balancing ions and the attraction to the basal surface determines the swelling behavior of smectites. Localization of charge in the *O* clay sheets supports swelling to 2W (and higher) while localization of the negative charge in the *T* sheets favors 1W (Figure 4 and 5).

We now consider the effects of layer charge localization and the interlayer ions on the CO₂-H₂O distributions. Figure 10 shows the calculated RDFs of carbon-water oxygen (C-O_w) and CO₂ oxygen – water hydrogen (O_{CO₂}-H_w) pairs for Na-MMT-CO₂-H₂O for both monolayer and bilayer conditions at $P = 125$ bar. The corresponding RDFs for Na-BEI-CO₂-H₂O (monolayer and bilayer) display qualitatively similar shapes and are not shown here. The C-O_w RDF displays only a weak shoulder near 3.1 Å, corresponding to coordination of water to carbon of CO₂. The shoulder is more pronounced in the bilayer than in the monolayer case, consistent with a larger number of water oxygens surrounding CO₂ molecules in the former. However, the RDF of carbon – basal oxygens indicates that the coordination number of basal oxygens is larger for the monolayer than for the bilayer, so on average the CO₂ molecules are surrounded by similar numbers of oxygens atoms in the monolayer and bilayer. This result is consistent with a prior analysis of the nearest-neighbor coordination numbers for CO₂ carbon atoms in hydrated Na-MMT.⁴³

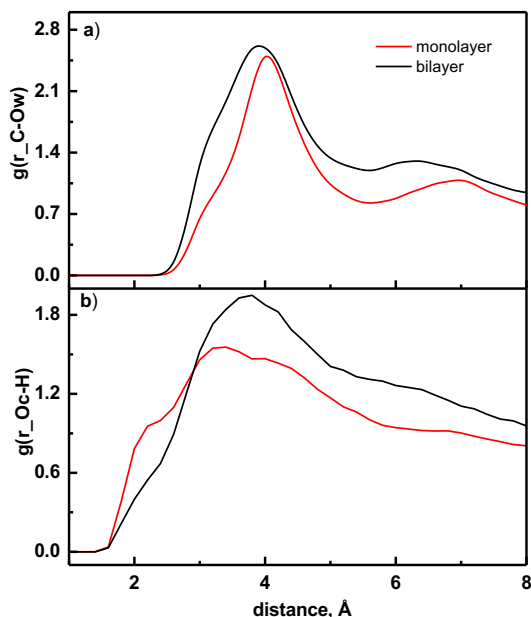
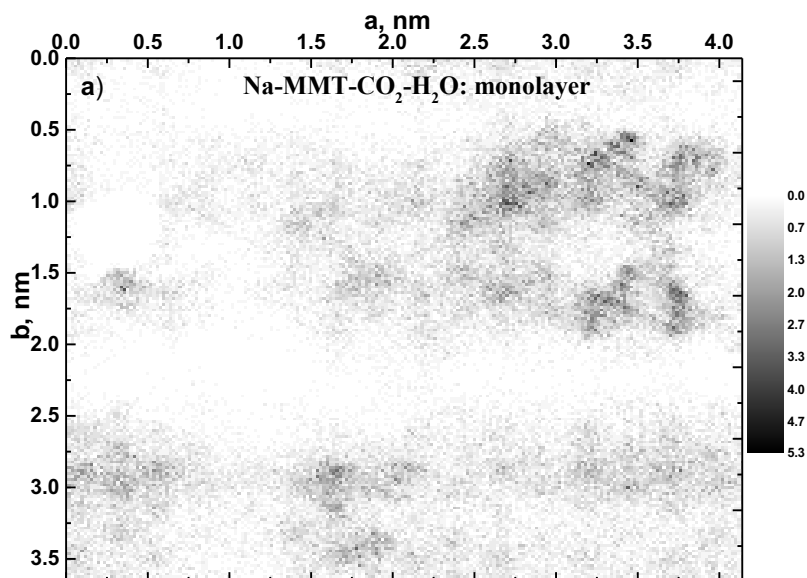


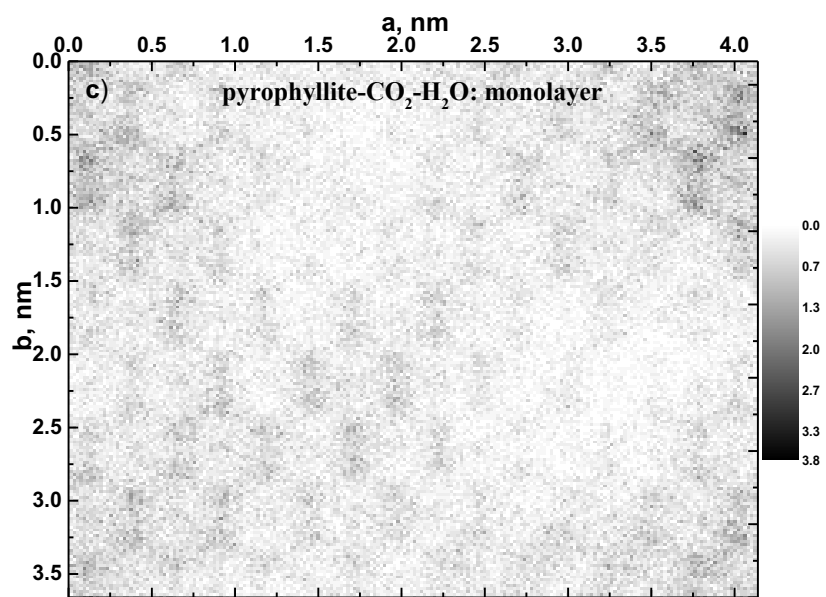
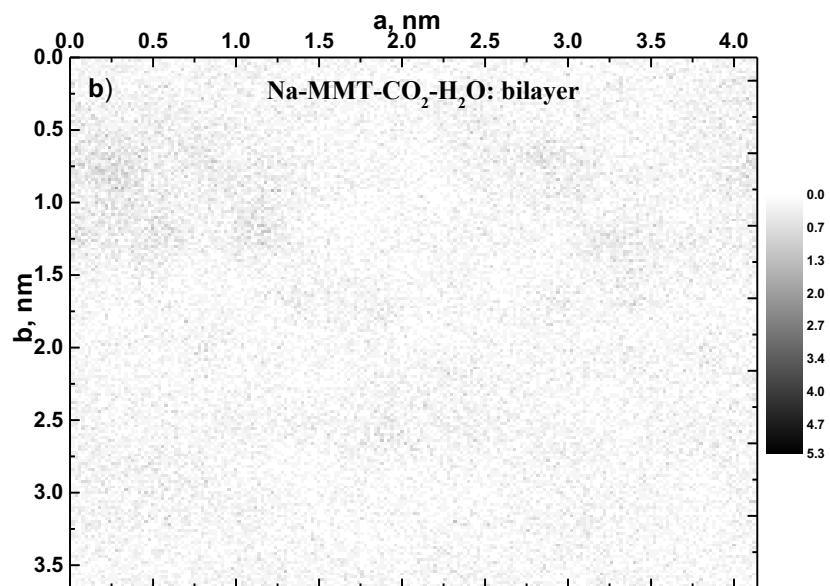
Figure 10: Radial distribution functions for **a)** carbon – water oxygen (water) and **b)** CO₂ oxygen – water hydrogen in Na-MMT-CO₂-H₂O at $P = 125$ bar and $T = 348.15$ K.

For the monolayer arrangement of Na-MMT-H₂O-CO₂, the O_{CO₂}-H_w RDF displays a well-defined shoulder near 2.3 Å, consistent with H-bond formation between H₂O and CO₂. This shoulder is much less pronounced for the bilayer. These results are consistent with the calculated average

lifetimes⁷⁸ of the H bonds between the O_{CO_2} atoms and the hydrogen atoms of the water molecules. The values are 1.3 and 0.2 ps ($P = 125$ bar, Na-MMT- CO_2 - H_2O) for the monolayer and the bilayer, respectively, implying stronger H-bonding in the former case. For Na-BEI- CO_2 - H_2O the corresponding computed lifetimes are 2.2 and 0.4 ps for 1W and 2W, respectively. The different lifetimes in the two clays can be related to details of the CO_2 distributions in the interlayers.

Figure 11 depicts number density maps for carbon dioxide molecules residing in a selected monolayer or bilayer of Na-MMT- CO_2 - H_2O , in a monolayer of Na-BEI- CO_2 - H_2O , and in pyrophyllite at a CO_2/H_2O composition corresponding to that of the monolayer of Na-MMT- CO_2 - H_2O . The maps were obtained by scanning the interlayer space to compute density distributions in planes parallel to the clay surfaces with a step size of 0.1 Å. Then, the distributions were projected onto the xy plane and averaged for 10 ns of simulation time.





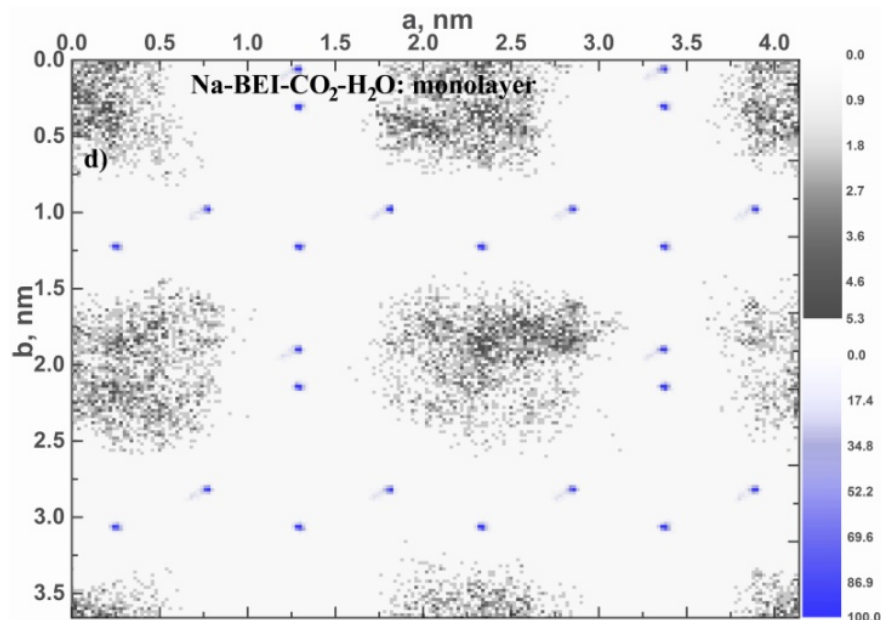


Figure 11. Density maps (number of molecules / nm³) showing carbon dioxide molecule distributions at P = 125 bar and T=348.15 K in the interlayer at d_{001} -spacing **a)** 12.5 Å for Na-MMT-CO₂-H₂O, **b)** 15.5 Å for Na-MMT-CO₂-H₂O, **c)** 12.5 Å for pyrophyllite, and **d)** 12.5 Å for Na-BEI-CO₂-H₂O with positions of Al substitutions in the adjacent tetrahedral layers given in blue. Results obtained by averaging over 10 ns of simulation time.

Pyrophyllite is a 2:1 dioctahedral phyllosilicate without charges on the mineral layers and, hence, no interlayer cations. The density map for pyrophyllite is included to provide additional insight into the effect of interlayer ions on the CO₂ distribution. For Na-MMT-CO₂-H₂O the distribution of CO₂ molecules is distinctly different in the monolayer and bilayer arrangements.

For the monolayer of Na-MMT-CO₂-H₂O, the density map reveals that the CO₂ molecules are non-uniformly distributed with respect to their XY coordinates and tend to conglomerate as represented by the dark regions in Figure 11. Analysis of distributions computed over various time frames shows that the clustered carbon dioxide molecules move over time in the interlayer. Migrating CO₂ clusters persist even in simulations carried out as long as for 50 ns. However, it is expected that averaged over sufficiently long times, the structure would smear out. The formation of CO₂ conglomerates in clay monolayers is supported by other studies that speculated that CO₂ enters the sub-1W interlayer "by pushing the structural units apart".^{4,64} Young and Smith¹⁰ reported that for Sr-MMT under sub 1W conditions the water molecule aggregates around the cations leaving voids. The voids can be filled by carbon dioxide in a "prop-and-fill" mechanism¹⁰ in which the clay is propped

open by hydrated cations making possible entrance of CO₂. In this work, it is found that the instantaneous spatial distribution of the clustered CO₂ molecules in Na-MMT is not correlated with the positions of the substitutions in the *O* sheets. However, it should be kept in mind that we have used a periodic rather than random distribution of substitution sites in the *T* or *O* layers, and that the distribution of CO₂ conglomerates could depend on the distribution of substitution sites. Earlier Monte Carlo simulations of cation distributions in the octahedral sheets of phyllosilicates suggest a tendency for Mg cations not to cluster in the Al/Mg systems⁷⁹ whereas in some montmorillonite samples Mg²⁺ were observed to form clusters.⁸⁰ Palin *et al.*⁸¹ using Monte Carlo simulations show short-range Al-Si ordering across the tetrahedral sheets of muscovite that depends on the Al:Si ratio and temperature. So, the ordering calculated in *T* sheets of muscovite supports the ordered placement of isomorphic substitutions in *T* sheets adopted in this work. In a previous study, we also found conglomerate formation of CO₂ for both Na- and Ca-MMT.³⁵ Thus, this behavior is not limited to clays with Na⁺ ions.

We hypothesize that the interlayer ions facilitate CO₂ conglomeration in the monolayer of the clay systems by "tying" up water molecules. To investigate this possibility, a simulation was conducted on pyrophyllite using the equilibrium CO₂/H₂O compositions computed for monolayer of Na-MMT-CO₂-H₂O at *P* = 125 bar. The resulting density distribution map, depicted in Figure 11, shows that CO₂ develops a periodic pattern reminiscent of ditrigonal rings of the basal surfaces. Thus, in the absence of interlayer ions, the tendency of CO₂ to conglomerate is suppressed, and its distribution is determined by the basal atoms of adjacent internal clay surfaces. In a previous paper devoted to turbostratic smectites, we showed that a rotational shift of one adjacent clay layer relative to the other creates Moiré patterns consisting of basal atoms.³⁵ Those patterns play a role in determining the distribution of interlayer species including carbon dioxide.

The distribution of CO₂ in the monolayer of Na-BEI-CO₂-H₂O (Figure 11) is particularly striking. The CO₂ molecules are clustered in the regions defined by the positions of the isomorphic substitutions in the *T* sheets (depicted by blue dots in Figure 11). CO₂ clearly tends to locate in the areas away from the charge originated from the substitutions, while the interlayer space near substitutions is occupied by water and hydrated cations. In the bilayer, the CO₂ density profile displays two-peaks (Figure 7) implying that the CO₂ molecules are exposed to the internal surfaces at

the comparable distances as in monolayer. Indeed, the corresponding distribution map (not shown) also reveals localized density regions controlled by the substitution positions, however, the structure is more smeared than in the monolayer. Obviously, in natural samples the substitution pattern could be irregular, and the CO₂ distribution would be more complex than shown in Figure 11. Nonetheless, the location of the layer charges in Na-BEI is a key factor in determining the CO₂ distribution in monolayer and bilayer. In Na-BEI-CO₂-H₂O the CO₂ motion is significantly restricted compared to the more mobile CO₂ conglomerates in Na-MMT-CO₂-H₂O. To quantify the transport properties of the interlayer species, diffusion coefficients were calculated and analyzed for both clays.

3.2.2. Diffusion of the interlayer species

Table 2 reports the computed diffusion coefficients for the interlayer species in Na-MMT, Na-BEI, and bulk phases obtained in this work and in other studies^{40,82-85} as well as from experimental measurements on similar systems. Both 3D and 2D (xy) values of the diffusion constants are given. In general, the diffusion constants for lateral motion of interlayer species are about 25-35% greater than those computed for 3D motion. As expected, the diffusion coefficients for CO₂, H₂O, and sodium ions increase in going from monolayer to bilayer arrangements, with the bilayer values being 5-10 times larger than the corresponding monolayer values. For Na-MMT-CO₂-H₂O the diffusion coefficients computed in this work are systematically higher than those calculated by Botan *et al.*⁴⁰ (Table 2). This is attributed to differences in the force fields used in the two works. Nevertheless, the calculated values of the diffusion constants of water from the two studies are close to the experimental result obtained using QENS spectroscopy. Also, our calculated diffusion constant for lateral motion of H₂O in Na-MMT is comparable to that measured for water in the interlayer region of Na-hectorite^{82,83} (a trioctahedral smectite with isomorphous substitution in the octahedral sheet that displays swelling properties similar to those of MMT).⁸⁴

Table 2: Diffusion coefficients ($\times 10^{-5}$ cm²/s) of water, carbon dioxide molecules, and Na⁺ cations in the interlayer spaces of Na-MMT and Na-BEI for the equilibrium CO₂/H₂O compositions corresponding to d_{001} -spacing of 12.5 and 15.5 Å at $T=347.15$ K.

	P, bar	H ₂ O		CO ₂		Na ⁺	
		D	D _{xy} ^a	D	D _{xy} ^a	D	D _{xy} ^a
Monolayer							
BEI-CO ₂ -H ₂ O	125	0.23(1)	0.32(2)	0.03(0)	0.04(0)	0.01(0)	0.01(0)
	25	0.33(3)	0.49(3)	0.05(1)	0.08(1)	0.01(0)	0.02(0)
MMT-CO ₂ -H ₂ O	125	0.41(3)	0.62(4)	0.28(3)	0.43(1)	0.11(1)	0.16(2)
	25	0.61(2)	0.91(4)	0.24(3)	0.35(4)	0.20(1)	0.27(1)

Bulk water	125	8.4(7)		10.3(8)		2.7(5)	
MMT-CO ₂ -H ₂ O ⁴⁰	125		0.32(2)		0.17(2)		0.13(2)
	25		0.51(2)		0.24(4)		0.19(2)
Hectorite-H ₂ O ⁸² (Expt., T=347K)	1		1.0(1)				0.13(2) ⁸⁵
Bilayer							
BEI-CO ₂ -H ₂ O	125	0.98(4)	1.48(4)	0.93(5)	1.50(6)	0.10(2)	0.14(2)
	25	1.39(5)	2.04(7)	1.29(4)	2.05(7)	0.11(3)	0.17(4)
MMT-CO ₂ -H ₂ O	125	2.39(3)	3.58(6)	1.55(6)	2.50(1)	1.12(2)	1.73(2)
	25	2.42(4)	3.63(7)	1.64(8)	2.81(5)	1.38(2)	1.92(3)
MMT-CO ₂ -H ₂ O ⁴⁰	125		3.2(1)		1.5(1)		1.4(1)
	25		3.5(1)		1.6(2)		1.3(1)
Hectorite-H ₂ O ⁸³ (Expt., T=347K)	1		2.2(2)				

^aD_{xy} denotes lateral a diffusion coefficient for motion parallel to clay surfaces.

The calculated diffusion coefficient of water in the bulk phase at is $8.4 \times 10^{-5} \text{ cm}^2/\text{s}$, in reasonable agreement with the experimental value of $5.97(6) \times 10^{-5} \text{ cm}^2/\text{s}$ ⁸⁶ at $T = 347 \text{ K}$. More importantly, the calculated diffusion constant for water in the bulk is 9-28 times greater than that for water in the monolayer and about 2-6 times larger than that of the bilayer for the two clays.⁴⁰ For both the monolayer and bilayer cases, the diffusion constant for water in Na-BEI-CO₂-H₂O is about two times smaller than for water in Na-MMT-CO₂-H₂O. Similarly, the measured diffusion constant for CO₂ in bulk water, $5.40 \pm 0.10 \times 10^{-5} \text{ cm}^2/\text{s}$ ($T = 348 \text{ K}$),⁸⁷ is about 1.5-3.0 times larger than for lateral motion of CO₂ in the clay bilayer and about an order of magnitude larger than that for lateral diffusion of CO₂ in the monolayer of Na-MMT-CO₂-H₂O. Due to the constrained motion of CO₂ in the monolayer of Na-BEI-CO₂-H₂O, the diffusion coefficient of CO₂ in that system is much smaller (by 5-10 times) than for Na-MMT-CO₂-H₂O.

Our calculated value of the Na⁺ diffusion constant in bulk water, $2.7 \times 10^{-7} \text{ cm}^2/\text{s}$, in reasonable agreement with the experimental value of $3.5 \times 10^{-5} \text{ cm}^2/\text{s}$.⁸⁸ It is also about twice as large as that for diffusion in Na⁺ in the bilayer and more than an order of magnitude larger than that for diffusion of Na⁺ in the monolayer of Na-MMT-CO₂-H₂O. Predictably, Na-BEI-CO₂-H₂O, for which the Na⁺ ions tend to be adsorbed at the internal surfaces, has much smaller Na⁺ diffusion constants than for Na-MMT-CO₂-H₂O in both the monolayer and bilayer cases. Kozaki *et al.*⁸⁹ reported a diffusion constant of $1.8 \times 10^{-6} \text{ cm}^2/\text{s}$ for interlayer sodium ions in the 2W hydration state of MMT at 323 K and 0.1-0.3 M concentrations of NaCl. Even though that value is in good agreement with that calculated in the present study for the 2W state of Na-MMT, direct comparison between calculated and measured ionic mobilities of smectite samples should be done with caution since the

experimental values can include substantial contributions from ions residing in pores and at external surfaces depending on experimental conditions and ionic strength.⁸⁹

IV. Conclusions

Molecular dynamics and multiphase Gibbs ensemble Monte Carlo simulations were carried out to study adsorption of carbon dioxide and water in the interlayer regions of Na-MMT and Na-BEI. The free energy calculations indicate that intercalation of pure CO₂ into the clay interlayers is not favorable, while pure H₂O adsorption may occur naturally at the (P , T) conditions relevant to carbon sequestration in deep geological formations. For Na-MMT-CO₂-H₂O the free energy of swelling shows two minima corresponding to monolayer and bilayer arrangements of the interlayer species, whereas for Na-BEI-CO₂-H₂O the expansion of the interlayer is limited to monolayer for both pure water and CO₂/water mixtures. This is a consequence of the strong interaction between the cations and the negatively charged clay layers.

The calculations predict the carbon dioxide concentrations in the interlayer of both clays greatly exceeding the solubility of CO₂ in bulk water at the (P , T) conditions of interest. In agreement with experiment, the maximum carbon dioxide adsorption occurs at the d_{001} -spacing range (11.5-12.5 Å) corresponding to the 1W hydration state. For both clays, CO₂ can fill the available space in sub-1W interlayer arrangements, resulting in expansion of d_{001} to 12.5 Å. The presence of interlayer cations leads to CO₂ conglomeration in the monolayer of Na-MMT-CO₂-H₂O. For Na-BEI-CO₂-H₂O, both the cations and the negative charges in the tetrahedral layers significantly impact the distributions of water and carbon dioxide molecules. CO₂ is driven away from the positions of isomorphic substitutions, whereas hydrated cations molecules are located close to Al³⁺/Si⁴⁺ substitution sites. The results showed that in smectites, hydrated cations and substitutions into tetrahedral sheets promote segregation of water and CO₂ in the interlayers and affects the ability of the clay minerals to retain carbon dioxide.

Not surprisingly, in the monolayer region of smectite clays, the mobilities of all interlayer species: water, CO₂, and Na⁺ are significantly retarded compared to the bulk phase. The corresponding diffusion constants in the bilayer regions are significantly less reduced compared to their values in bulk water. The most prominent reduction in mobility is found for CO₂ and Na⁺ in Na-BEI-CO₂-H₂O.

The simulations predict that at equilibrium with a CO₂-bearing aquifer, carbon dioxide intercalation into hydrated clay phases is accompanied by expansion of the interlayer distance causing increase of clay volume, which, in turn, influences the porosity and permeability of formations enriched in expandable clay minerals. The greater solubility of CO₂ in the interlayer region of smectites than in bulk water suggests that smectite minerals are good candidates for carbon dioxide storage.

Acknowledgment

This technical effort was performed in support of the National Energy Technology Laboratory's ongoing research in Subtask 4000.4.641.061.002.254 under the RES contract DE-FE0004000. The simulations were carried out on NETL's High-Performance Computer for Energy and the Environment (HPCEE) and on computers in the University of Pittsburgh's Center for Simulation and Modeling.

Disclaimer

This project was funded by the Department of Energy, National Energy Technology Laboratory, an agency of the United States Government, through a support contract with AECOM. Neither the United States Government nor any agency thereof, nor any of their employees, nor AECOM, nor any of their employees, makes any warranty, expressed or implied, or assumes any legal liability or responsibility for the accuracy, completeness, or usefulness of any information, apparatus, product, or process disclosed, or represents that its use would not infringe privately owned rights. Reference herein to any specific commercial product, process, or service by trade name, trademark, manufacturer, or otherwise, does not necessarily constitute or imply its endorsement, recommendation, or favoring by the United States Government or any agency thereof. The views and opinions of authors expressed herein do not necessarily state or reflect those of the United States Government or any agency thereof.

References

- (1) Houghton, J. *Global Warming: The Complete Briefing*; Cambridge University Press: Cambridge, U.K., 2009.
- (2) Benson, S. M.; Cole, D. R. CO₂ sequestration in deep sedimentary formations. *Elements* **2008**, *4*, 325-331.
- (3) Giesting, P.; Guggenheim, S.; Koster van Groos, A. F.; Busch, A. Interaction of carbon dioxide with Na-exchanged montmorillonite at pressures to 640 bars: implications for CO₂ sequestration. *Int. J. Greenhouse Gas Control* **2012**, *8*, 73-81.
- (4) Giesting, P.; Guggenheim, S.; Koster van Groos, A. F.; Busch, A. X-ray diffraction study of K- and Ca-exchanged montmorillonites in CO₂ atmospheres. *Environ. Sci. Technol.* **2012**, *46*, 5623-5630.
- (5) Rother, G.; Ilton, E. S.; Wallacher, D.; Hauß, T.; Schaef, H. T.; Qafoku, O.; Rosso, K. M.; Felmy, A. R.; Krukowski, E. G.; Stack, A. G.; et al. CO₂ sorption to subsingle hydration layer montmorillonite clay studied by excess sorption and neutron diffraction measurements. *Environ. Sci. Technol.* **2012**, *47*, 205-211.
- (6) Ilton, E. S.; Schaef, H. T.; Qafoku, O.; Rosso, K. M.; Felmy, A. R. In situ X-ray diffraction study of Na⁺ saturated montmorillonite exposed to variably wet super critical CO₂. *Environ. Sci. Technol.* **2012**, *46*, 4241-4248.
- (7) Norrish, K. The swelling of montmorillonite. *Discuss. Faraday Soc.* **1954**, *18*, 120-134.
- (8) Hensen, E. J.; Smit, Why clays swell. *B. J. Phys. Chem. B* **2002**, *106*, 12664-12667.
- (9) Berend, I.; Cases, J.; Francois, M.; Uriot, J.; Michot, L.; Masion, A.; Thomas, F. Mechanism of adsorption and desorption of water vapor by homoionic montmorillonites: 2. the Li, Na, K, Rb and Cs⁺-exchanged forms. *Clays Clay Miner.* **1995**, *43*, 324-336.
- (10) Young, D. A.; Smith, D. E. Simulations of clay mineral swelling and hydration: dependence upon interlayer ion size and charge. *J. Phys. Chem. B* **2000**, *104*, 9163-9170.
- (11) Douillard, J.-M.; Lantenois, S.; Prelot, B.; Zajac, J.; Henry, M. Study of the influence of location of substitutions on the surface energy of dioctahedral smectites. *J. Colloid Interface Sci.* **2008**, *325*, 275-281.
- (12) Skipper, N.; Refson, K.; McConnell, J. Computer simulation of interlayer water in 2:1 clays. *J. Chem. Phys.* **1991**, *94*, 7434-7445.
- (13) Skipper, N.; Chang, F.-R. C.; Sposito, G. Monte Carlo simulation of interlayer molecular structure in swelling clay minerals. i: Methodology. *Clays Clay Miner.* **1995**, *43*, 285-293.

- (14) Skipper, N.; Sposito, G.; Chang, F.-R. C. Monte Carlo simulation of interlayer molecular structure in swelling clay minerals. 2. Monolayer hydrates. *Clays Clay Miner.* **1995**, *43*, 294-303.
- (15) Delville, A. Modeling the clay-water interface. *Langmuir* **1991**, *7*, 547-555.
- (16) Delville, A. Structure of liquids at a solid interface: an application to the swelling of clay by water. *Langmuir* **1992**, *8*, 1796-1805.
- (17) Delville, A. Structure and properties of confined liquids: a molecular model of the clay-water interface. *J. Phys. Chem.* **1993**, *97*, 9703-9712.
- (18) Chang, F.-R. C.; Skipper, N.; Sposito, G. Computer simulation of interlayer molecular structure in sodium montmorillonite hydrates. *Langmuir* **1995**, *11*, 2734-2741.
- (19) Bordarier, P.; Rousseau, B.; Fuchs, A. H. Rheology of model confined ultrathin fluid films. i. statistical mechanics of the surface force apparatus experiments. *J. Chem. Phys.* **1997**, *106*, 7295-7302.
- (20) Marry, V.; Turq, P.; Cartailier, T.; Levesque, D. Microscopic simulation of structure and dynamics of water and counterions in a monohydrated montmorillonite. *J. Chem. Phys.* **2002**, *117*, 3454-3463.
- (21) Suter, J. L.; Sprik, M.; Boek, E. S. Free energies of absorption of alkali ions onto beidellite and montmorillonite surfaces from constrained molecular dynamics simulations. *Geochim. Cosmochim. Acta* **2012**, *91*, 109-119.
- (22) Teppen, B. J.; Rasmussen, K.; Bertsch, P. M.; Miller, D. M.; Schaefer, L. Molecular dynamics modeling of clay minerals. 1. Gibbsite, kaolinite, pyrophyllite, and beidellite. *J. Phys. Chem. B* **1997**, *101*, 1579-1587.
- (23) Greathouse, J. A.; Cygan, R. T. Water structure and aqueous uranyl (VI) adsorption equilibria onto external surfaces of beidellite, montmorillonite, and pyrophyllite: Results from molecular simulations. *Environ. Sci. Technol.* **2006**, *40*, 3865-3871.
- (24) Fu, M.; Zhang, Z.; Low, P. Changes in the properties of a montmorillonite-water system during the adsorption and desorption of water: hysteresis. *Clays Clay Miner.* **1990**, *38*, 485-492.
- (25) Cygan, R. T.; Liang, J.-J.; Kalinichev, A. G. Molecular models of hydroxide, oxyhydroxide, and clay phases and the development of a general force field. *J. Phys. Chem. B* **2004**, *108*, 1255-1266.
- (26) Smith, D. E. Molecular computer simulations of the swelling properties and interlayer structure of cesium montmorillonite. *Langmuir* **1998**, *14*, 5959-5967.

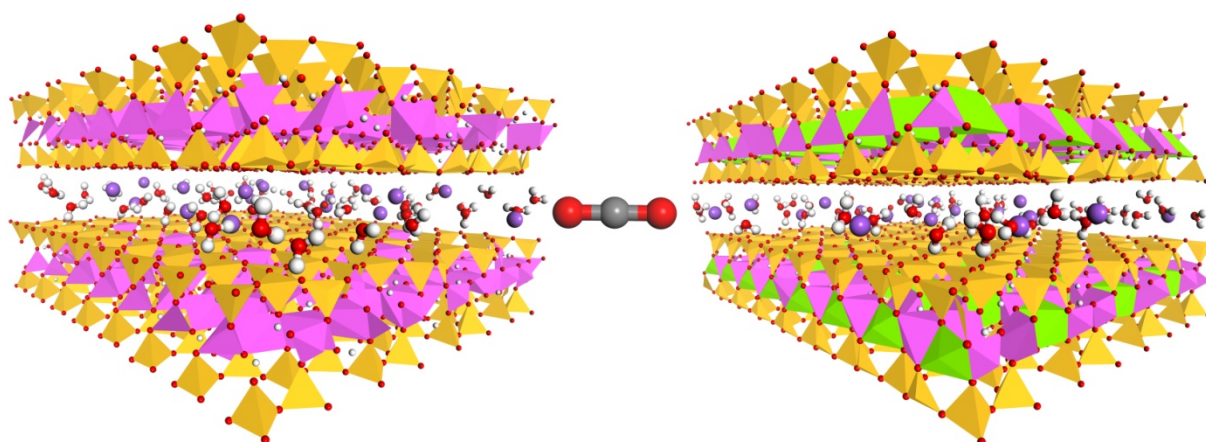
- (27) Mooney, R.; Keenan, A.; Wood, L. Adsorption of water vapor by montmorillonite. i. Heat of desorption and application of BET theory. *J. Am. Chem. Soc.* **1952**, *74*, 1367-1371.
- (28) Calvet, R. Hydratation de la Montmorillonite et Diffusion des Cations Compensateurs. Université VI, Faculté des Sciences Physiques, 1972.
- (29) Whitley, H. D.; Smith, D. E. Free energy, energy, and entropy of swelling in Cs-, Na-, and Sr-montmorillonite clays. *J. Chem. Phys.* **2004**, *120*, 5387-5395.
- (30) Schaefer, H. T.; Ilton, E. S.; Qafoku, O.; Martin, P. F.; Felmy, A. R.; Rosso, K. M. In situ XRD study of Ca²⁺-saturated montmorillonite (Stx-1) exposed to anhydrous and wet supercritical carbon dioxide. *Int. J. Greenhouse Gas Control* **2012**, *6*, 220-229.
- (31) Odriozola, G.; Aguilar, J.; Lopez-Lemus, J. Na-montmorillonite hydrates under ethane rich reservoirs: NP_{zz}T and μ P_{zz}T simulations. *J. Chem. Phys.* **2004**, *121*, 4266-4275.
- (32) Billefont, P.; Coasne, B.; De Weireld, G. An experimental and molecular simulation study of the adsorption of carbon dioxide and methane in nanoporous carbons in the presence of water. *Langmuir* **2010**, *27*, 1015-1024.
- (33) Ferrage, E.; Sakharov, B. A.; Michot, L. J.; Delville, A.; Bauer, A.; Lanson, B.; Grangeon, S.; Frapper, G.; Jimenez-Ruiz, M.; Cuello, G. J. Hydration properties and interlayer organization of water and ions in synthetic Na-smectite with tetrahedral layer charge. Part 2. Toward a precise coupling between molecular simulations and diffraction data. *J. Phys. Chem. C* **2011**, *115*, 1867-1881.
- (34) Zhang, G.; Al-Saidi, W. A.; Myshakin, E. M.; Jordan, K. D. Dispersion-corrected density functional theory and classical force field calculations of water loading on a pyrophyllite(001) surface. *J. Phys. Chem. C* **2012**, *116*, 17134-17141.
- (35) Cygan, R. T.; Romanov, V. N.; Myshakin, E. M. Molecular simulation of carbon dioxide capture by montmorillonite using an accurate and flexible force field. *J. Phys. Chem. C* **2012**, *116*, 13079-13091.
- (36) Myshakin, E. M.; Saidi, W. A.; Romanov, V. N.; Cygan, R. T.; Jordan, K. D. Molecular dynamics simulations of carbon dioxide intercalation in hydrated Na-montmorillonite. *J. Phys. Chem. C* **2013**, *117*, 11028-11039.
- (37) Churakov, S. V. Mobility of Na and Cs on montmorillonite surface under partially saturated conditions. *Environ. Sci. Technol.* **2013**, *47*, 9816-9823.
- (38) Myshakin, E.; Makaremi, M.; Romanov, V. N.; Jordan, K. D.; Guthrie, G. D. Molecular dynamics simulations of turbostratic dry and hydrated montmorillonite with intercalated carbon dioxide. *J. Phys. Chem. A* **2014**, *118*, 7454-7468.

- (39) Titiloye, J.; Skipper, N. Computer simulation of the structure and dynamics of methane in hydrated Na-smectite clay. *Chem. Phys. Lett.* **2000**, *329*, 23-28.
- (40) Titiloye, J. O.; Skipper, N. T. Monte Carlo and molecular dynamics simulations of methane in potassium montmorillonite clay hydrates at elevated pressures and temperatures. *J. Colloid Interface Sci.* **2005**, *282*, 422-427.
- (41) Liu, X.-D.; Lu, X.-C. A thermodynamic understanding of clay-swelling inhibition by potassium ions. *Angewandte Chemie International Edition* **2006**, *45*, 6300-6303.
- (42) Rotenberg, B.; Morel, J.-P.; Marry, V.; Turq, P.; Morel-Desrosiers, N. On the driving force of cation exchange in clays: Insights from combined microcalorimetry experiments and molecular simulation. *Geochim. Cosmochim. Acta* **2009**, *73*, 4034-4044.
- (43) Botan, A.; Rotenberg, B.; Marry, V.; Turq, P.; Noetinger, B. Carbon dioxide in montmorillonite clay hydrates: thermodynamics, structure, and transport from molecular simulation. *J. Phys. Chem. C* **2010**, *114*, 14962-14969.
- (44) Panagiotopoulos, A. Z. Adsorption and capillary condensation of fluids in cylindrical pores by Monte Carlo simulation in the Gibbs ensemble. *Mol. Phys.* **1987**, *62*, 701-719.
- (45) McGrother, S. C.; Gubbins, K. E. Constant pressure Gibbs ensemble Monte Carlo simulations of adsorption into narrow pores. *Mol. Phys.* **1999**, *97*, 955-965.
- (46) Diestler, D.; Schoen, M.; Curry, J. E.; Cushman, J. H. Thermodynamics of a fluid confined to a slit pore with structured walls. *J. Chem. Phys.* **1994**, *100*, 9140-9146.
- (47) Lopes, J. C.; Tildesley, D. Multiphase equilibria using the Gibbs ensemble Monte Carlo method. *Mol. Phys.* **1997**, *92*, 187-196.
- (48) Martin, M. G.; Siepmann, J. I. Calculating Gibbs free energies of transfer from Gibbs ensemble Monte Carlo simulations. *Theor. Chem. Acc.* **1998**, *99*, 347-350.
- (49) Liu, A.; Beck, T. L. Vapor-liquid equilibria of binary and ternary mixtures containing methane, ethane, and carbon dioxide from Gibbs ensemble simulations. *J. Phys. Chem. B* **1998**, *102*, 7627-7631.
- (50) Kristof, T.; Vorholz, J.; Maurer, G. Molecular simulation of the high-pressure phase equilibrium of the system carbon dioxide-methanol-water. *J. Phys. Chem. B* **2002**, *106*, 7547-7553.
- (51) Carrero-Mantilla, J.; Llano-Restrepo, M. Vapor-liquid equilibria of the binary mixtures nitrogen+methane, nitrogen+ethane and nitrogen+carbon dioxide, and the ternary mixture nitrogen+methane+ethane from Gibbs-ensemble molecular simulation. *Fluid Phase Equilib.* **2003**, *208*, 155-169.

- (52) Zhang, L.; Siepmann, J. I. Pressure dependence of the vapor-liquid-liquid phase behavior in ternary mixtures consisting of n-alkanes, n-perfluoroalkanes, and carbon dioxide. *J. Phys. Chem. B* **2005**, *109*, 2911-2919.
- (53) Loewenstein, W. The distribution of aluminum in the tetrahedra of silicates and aluminates. *Am. Mineral.* **1954**, *39*, 92-96.
- (54) Berendsen, H. J.; Postma, J. P.; Van Gunsteren, W. F.; Hermans, J. Interaction models for water in relation to protein hydration. *Intermolecular Forces*: Springer 1981, 331-342.
- (55) Allen, M. P.; Tildesley, D. J. *Computer Simulation of Liquids*: Clarendon, Oxford, 1989.
- (56) Wiebe, R. The binary system carbon dioxide-water under pressure. *Chem. Rev.* **1941**, *29*, 475-481.
- (57) Gillespie, P. C.; Wilson, G. M. *Vapor-Liquid and Liquid-Liquid Equilibria: Water- Methane, Water-Carbon Dioxide, Water-Hydrogen Sulfide, Water-Npentane, Water-Methane-Npentane*: Gas Processors Association, 1982.
- (58) Vorholz, J.; Harismiadis, V.; Rumpf, B.; Panagiotopoulos, A.; Maurer, G. Vapor+liquid equilibrium of water, carbon dioxide, and the binary system, water+carbon dioxide, from molecular simulation. *Fluid Phase Equilib.* **2000**, *170*, 203-234.
- (59) McDonald, I. NPT-ensemble Monte Carlo calculations for binary liquid mixtures. *Mol. Phys.* **1972**, *23*, 41-58.
- (60) Mooij, G.; Frenkel, D.; Smit, B. Direct simulation of phase equilibria of chain molecules. *J. Phys.: Condens. Matter* **1992**, *4*, L255.
- (61) Martin, M. G.; Frischknecht, A. L. Using arbitrary trial distributions to improve intramolecular sampling in configurational-bias Monte Carlo. *Mol. Phys.* **2006**, *104*, 2439-2456.
- (62) Frenkel, D.; Smit, B. *Understanding Molecular Simulation: From Algorithms to Applications*: Academic press, 2001; Vol. 1.
- (63) MCCCSTowhee version 7.0.6. <http://towhee.sourceforge.net>, Accessed: 2014-07-1.
- (64) Nôse, S. A molecular dynamics method for simulations in the canonical ensemble. *Mol. Phys.* **1984**, *52*, 255-268.
- (65) Hoover, W. G. Canonical dynamics: equilibrium phase-space distributions. *Phys. Rev. A* **1985**, *31*, 1695.
- (66) Van Gunsteren, W.; Berendsen, H. A leap-frog algorithm for stochastic dynamics. *Mol. Simul.* **1988**, *1*, 173-185.
- (67) Van Der Spoel, D.; Hess B.; Lindahl E. The GROMACS development team, GROMACS

- User Manual version 4.6.5, www.gromacs.org. 2013. Accessed: 2014-09-28.
- (68) Loring, J. S.; Schaefer, H. T.; Turcu, R. V.; Thompson, C. J.; Miller, Q. R.; Martin, P. F.; Hu, J.; Hoyt, D. W.; Qafoku, O.; Ilton, E. S.; et al. In situ molecular spectroscopic evidence for CO₂ intercalation into montmorillonite in supercritical carbon dioxide. *Langmuir* **2012**, *28*, 7125-7128.
- (69) Cases, J.; Berend, I.; Besson, G.; Francois, M.; Uriot, J.; Thomas, F.; Poirier, J. Mechanism of adsorption and desorption of water vapor by homoionic montmorillonite. 1. The sodium-exchanged form. *Langmuir* **1992**, *8*, 2730-2739.
- (70) Karaborni, S.; Smit, B.; Heidug, W.; Urai, J.; Van Oort, E. The swelling of clays: molecular simulations of the hydration of montmorillonite. *Science* **1996**, *271*, 1102.
- (71) Chavez-Paez, M.; Van Workum, K.; De Pablo, L.; De Pablo, J. J. Monte Carlo simulations of Wyoming sodium montmorillonite hydrates. *J. Chem. Phys.* **2001**, *114*, 1405-1413.
- (72) Anderson, R.; Ratcliffe, I.; Greenwell, H.; Williams, P.; Clifton, S.; Coveney, P. Clay swelling: a challenge in the oil field. *Earth-Sci. Rev.* **2010**, *98*, 201-216.
- (73) Smith, D. E.; Wang, Y.; Whitley, H. D. Molecular simulations of hydration and swelling in clay minerals. *Fluid Phase Equilib.* **2004**, *222*, 189-194.
- (74) Klopogge, J. T.; Jansen, J. B. H.; Geus, J. W. Characterization of synthetic Na-beidellite. *Clays Clay Miner.* **1990**, *38*, 409-414.
- (75) Loring, J. S.; Ilton, E. S.; Chen, J.; Thompson, C. J.; Martin, P. F.; Benezeth, P.; Rosso, K. M.; Felmy, A. R.; Schaefer, H. T. In situ study of CO₂ and H₂O partitioning between Na-montmorillonite and variably wet supercritical carbon dioxide. *Langmuir* **2014**, *30*, 6120-6128.
- (76) Ansell, S.; Barnes, A.; Mason, P.; Neilson, G.; Ramos, S. X-ray and neutron scattering studies of the hydration structure of alkali ions in concentrated aqueous solutions. *Biophys. Chem.* **2006**, *124*, 171-179.
- (77) Soper, A. K.; Weckstrom, K. Ion solvation and water structure in potassium halide aqueous solutions. *Biophys. Chem.* **2006**, *124*, 180-191.
- (78) Khalack, J.; Lyubartsev, A. Car-Parrinello molecular dynamics simulations of Na⁺-Cl⁻ ion pair in liquid water. *Condens. Matter Phys.* **2004**, *7*, 683-698.
- (79) Palin, E.J.; Dove, M. T.; Hernández-Laguna, A.; Santz-Díaz, A. A computational investigation of the Al/Fe/Mg order-disorder behavior in the dioctahedral sheet of phyllosilicates. *Am. Mineral.*, **2004**, *89*, 164-175.
- (80) Muller, F.; Besson, G.; Manceau, A.; Drits, V. A. Distribution of isomorphous cations within

- octahedral sheets in montmorillonite from Camp-Bertaux. *Phys. Chem. Miner*, **1997**, *24*, 159-166.
- (81) Palin, E.J.; Dove, M. T.; Redfern, S. A.T.; Bosenick, A.; Santz-Díaz, C. I.; Warren, M. C. Computational study of tetrahedral Al-Si ordering in muscovite. *Phys. Chem. Miner*, **2001**, *28*, 534-544.
- (82) Marry, V.; Dubois, E.; Malikova, N.; Durand-Vidal, S.; Longeville, S.; Breu, J. Water dynamics in hectorite clays: influence of temperature studied by coupling neutron spin echo and molecular dynamics. *Environ. Sci. Technol.* **2011**, *45*, 2850-2855.
- (83) Marry, V.; Dubois, E.; Malikova, N.; Breu, J.; Haussler, W. Anisotropy of water dynamics in clays: insights from molecular simulations for experimental QENS analysis. *J. Phys. Chem. C* **2013**, *117*, 15106-15115.
- (84) Malikova, N.; Cadene, A.; Dubois, E.; Marry, V.; Durand-Vidal, S.; Turq, P.; Breu, J.; Longeville, S.; Zanotti, J. M. Water diffusion in a synthetic hectorite clay studied by quasi-elastic neutron scattering. *J. Phys. Chem. C* **2007**, *111*, 17603-17611.
- (85) Marry, V.; Malikova, N.; Cadene, A.; Dubois, E.; Durand-Vidal, S.; Turq, P.; Breu, J.; Longeville, S.; Zanotti, J. M. Water diffusion in a synthetic hectorite by neutron scattering-beyond the isotropic translational model. *J. Phys.: Condens. Matter* **2008**, *20*, 104205.
- (86) Holz, M.; Heil, S. R.; Sacco, A. Temperature-dependent self-diffusion coefficients of water and six selected molecular liquids for calibration in accurate ¹H NMR PFG measurements. *Phys. Chem. Chem. Phys.* **2000**, *2*, 4740-4742.
- (87) Lindeberg, E.; Wessel-Berg, D. Vertical convection in an aquifer column under a gas cap of CO₂. *Energy Convers. Manage.* **1997**, *38*, S229- S234.
- (88) Stokes, R.; Robinson, R. Electrolyte solutions. *Butterworths, London* **1959**.
- (89) Kozaki, T.; Fujishima, A.; Sato, S.; Ohashi, H. Self-diffusion of sodium ions in compacted sodium montmorillonite. *Nucl. Technol.* **1998**, *121*, 63-69.



TOC figure. Beidellite (left) and Montmorillonite (right) structures with intercalated water molecules and sodium ions. Carbon dioxide molecule shown in the middle. The atom color coding: purple, red, white, grey, yellow, pink and green for Na, O, H, C, Si, Al and Mg, respectively.